HEFAT2014
10th International Conference on Heat Transfer, Fluid Mechanics and Thermodynamics
14 – 16 July 2014
Orlando, Florida
Paper # 1569878041

NUMERICAL MODELING OF THE TRANSIENT TEMPERATURE RISE DURING BALL-ON-DISK SCUFFING TESTS

Rebeca Lumbreras, Monica Majcher, Laila Guessous*, Gary Barber, J. David Schall, and Qian Zou
*Author for correspondence
Department of Mechanical Engineering,
Oakland University
Rochester, MI 48309
USA
E-mail: guessous@oakland.edu

ABSTRACT

Scuffing is a form of surface damage and wear that occurs in inadequately-lubricated tribosystems that causes catastrophic damage on tribological surfaces and usually results in the need for part replacement. As a major cause of failure in automotive and other mechanical components, scuffing has been the focus of much research to elucidate its fundamental underpinnings. One of the characteristics of scuffing is an increase in the coefficient of friction and in the surface temperature of the contacting parts. In this paper, we report on ongoing numerical work focused on modeling the transient temperature rise that occurs in a workpiece during a ball-on-disk tribometer test. In such a test, a load is applied to a stationary ball which is placed in contact with a rotating disk. Inputs to the numerical thermal model come from experimental and numerical contact mechanics tests. Results for both the bulk disk temperature, as well as the surface flash temperature under different loading conditions are presented and discussed.

INTRODUCTION

Scuffing can be defined as a sudden catastrophic failure of the lubricated sliding surfaces; it is characterized by a sudden rise in friction, contact temperature, and vibration/noise, resulting in surface roughening and loss of surface integrity and functionality [1]. There are two main reasons that make scuffing an important research subject; first its unpredictability and catastrophic occurrence and second the consequent overdesign of parts to avoid scuffing.

Scuffing on parts with relative motion has been a subject of research for many years. Many scuffing models have been developed during this time trying to predict scuffing and understand the specific causes that generate it. Valuable information has been gathered about scuffing but there is still little agreement on a scuffing model or on a set of test or environment conditions in which scuffing occurs. Therefore engineers often overdesign critical parts to avoid this sudden and catastrophic failure, resulting in what may be unnecessary additional costs or weight of the parts.

Most researchers agree that scuffing is thermal in nature and frictional heating due to interacting asperities is an important parameter [2]. This is hence the perspective taken in this ongoing investigation. One of the earliest models along these lines is the one proposed by Block in 1937 [3]. One of the important contributions of his critical temperature model was the observation that the critical temperature was a combination of the contacting materials' bulk temperature and the instantaneous flash temperature rise occurring as the surface passed through the contact [3]. Later Dyson proposed that when a critical temperature is reached the viscosity suddenly falls causing the elastohydrodynamic lubrication (EHL) film to collapse promoting scuffing [4]. There are several studies based on lubricant desorption models, which suggest a critical temperature associated with desorption from the metallic surfaces of polar molecules in the lubricant [5, 6]. Other theories are based on the lubricant's ability to withstand thermal and oxidative degradation [7]. On the other hand, many researchers explain the onset of scuffing by mechanisms of asperity interaction and plastic flow. Repeated cyclic plastic deformation of asperities causes them to break away by plastic fatigue. The particles formed agglomerate, work harden and eventually the majority of the contact load is carried by a few larger particles, resulting in large contact stress. This causes an increase in temperature, which alters the protective films, resulting eventually in scuffing [8]. Lastly, frictional power intensity theories, which define the rate of heat dissipation within the contact divided by the contact area, instead use a scuffing criterion which postulates that scuffing will occur when the level of frictional heat generation reaches a critical level [9].

The goal of the present ongoing study is to use a combination of experimental and numerical analyses to gain a better understanding of the scuffing phenomenon. In this paper, we report on the development of a numerical thermal model that makes use of data from experimental ball-on-disk tribometer tests and numerical contact mechanics simulations to predict the transient temperature rise on the surface of and within a workpiece. Sample results for both the bulk disk temperature, as well as the surface flash temperature of a 4140 steel sample under different loading conditions are presented and discussed.

GENERAL METHODOLOGY

In order to obtain the necessary inputs for the thermal simulations, the following multifaceted general procedure was followed:

- Ball-on-disk tribometer tests were conducted on several material samples, including 4140 steel [10]. Two types of tests, wear tests and scuffing tests were conducted. Data collected included the applied load, coefficient of friction (COF) and rotation velocity. In addition, wear track surface profiles were measured after the tests were completed and the microstructure of the surface and subsurface of the test samples was analyzed before and after the tests.
- Data from the experimental tests is next input into a numerical contact mechanics model to, among other things calculate subsurface stresses and strains, contact pressure distribution and contact area at the end of the test.
- COF, rotation (sliding) velocity, contact pressure and contact area are next needed for the numerical models used to predict the temperature rise of the workpiece under various testing and loading conditions. Due to the small size of the contact area relative to the rest of the workpiece, very fine numerical meshes are needed to capture the spatial and temporal temperature rise in the contact area. Most of the temperature rise occurs near the contact area surface, so coarser meshes may be used in the disk away from the contact area. However, numerical accuracy requirements dictate that the mesh size be increased gradually from the contact area outwards, resulting in extremely large systems of equations and prohibitively slow program running time. For this reason, a multiscale modelling approach was used for the temperature prediction. First, an average contact pressure is used in simulations of the evolution of the three-dimensional temperature of the sample during a test to obtain a representative bulk temperature. Results from this first model, along with the pressure distribution in the contact area obtained from the contact mechanics model are then used in a second 3-D simulation that focuses on a much smaller computational domain in the vicinity of the contact area and computes the evolution of the local flash temperature over very short periods of time.

EXPERIMENTAL SETUP

Test setup

A ball-on-disk test is commonly used when studying scuffing phenomena. As shown in Figure 1, a normal load is applied to a bearing ball which is in contact with a rotating sample. Testing can be done in one of two ways: One, maintain a constant rotating velocity of the sample and increase the load periodically until scuffing happens; or two, apply a constant load and increase the angular velocity until scuffing occurs. For this work the first approach was taken.

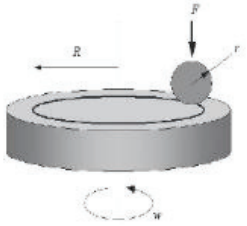

Figure 1: Schematic of ball-on-disk type test.

The machine used to run the tests was a UMT3 tribometer from CETR, with a rotary drive, a 100kg load sensor and a suspension. An adaptor to hold the bearing ball stationary was attached to the suspension on the load sensor. The flatness and the parallelism of the two sides of the sample were verified with a deflection gage before each test to ensure stability when the load was applied. All of the tests were run at an ambient temperature of 295 K (22°C), and the coefficient of friction (COF) was monitored and recorded throughout the test.

The AISI 4140 alloy steel sample rotated at a constant speed of 700rpm, with a wear track radius of 21.75mm which translates into a tangential velocity V of about 1.6m/s. A step in the load of 13.34 N was applied to workpiece every two minutes. Before starting the test, 4ml of lubricant were added to the surface of the sample; an additional 1ml of the lubricant in the part holder was moved back to the surface of the sample every 2 minutes.

Two types of tests were run: wear and scuffing tests. The scuffing tests are run at a constant linear velocity and a step load of 13.34 N was applied every 2 minutes until the coefficient of friction suddenly jumped, usually over values of 0.2; this sudden increase in the COF is an indication of scuffing. The load that was applied to the sample when it scuffed was defined as the scuffing load. Figure 2 shows an example load and COF graph for a scuffing test.

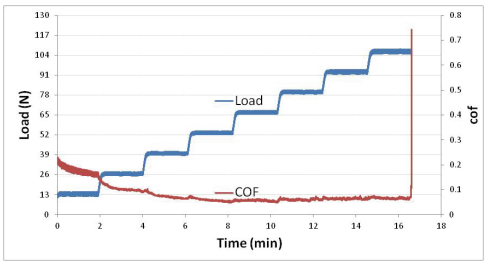

Figure 2: Example of a scuffing test (blue indicates load versus time; red indicates coefficient of friction versus time)

The wear tests followed the same setup as the scuffing tests but instead of proceeding until the COF jumped, they were stopped at specific times. For instance, as shown in Figure 3,

the 13.34 N wear test was stopped after running for 2 minutes with a load 13.34 N. The 26.69 N wear test was stopped after first running for 2 minutes with a load of 13.34 N and 2 minutes with a load of 26.69 N. Similarly, the 53.37 N wear test was stopped after first running 2 minutes with a load of 13.34 N, 2 minutes with a load of 26.69 N, 2 minutes with a load of 40.03 N and 2 minutes with a load of 53.37 N.

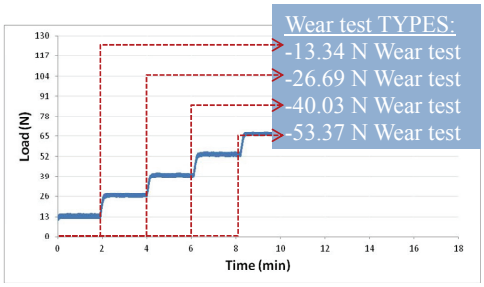

Figure 3: Wear tests are stopped at specific times after undergoing various step loads.

The goal from the scuffing tests was to determine a scuffing load window for this combination of material and test conditions. The average scuffing load measured from the tests was 66.72 N (15lb). For this investigation four different load wear tests were performed as described before. The purpose of the wear tests was to provide the surface data, wear and friction information for each step load, which could then be fed into the thermal models to calculate the temperature evolution of the contact area during a ball-on-disk scuffing test.

Figure 4 shows the value of the coefficient of friction, as well as the step load versus time for the 40.03 N and 53.37 N wear tests. The coefficient of friction can be seen to start with a value close to 0.12 in both cases, then, once most of the highest asperities were worn out, it can be seen to decrease to values under 0.1. Note how the sudden increases in load are initially accompanied by increases in the coefficient of friction.

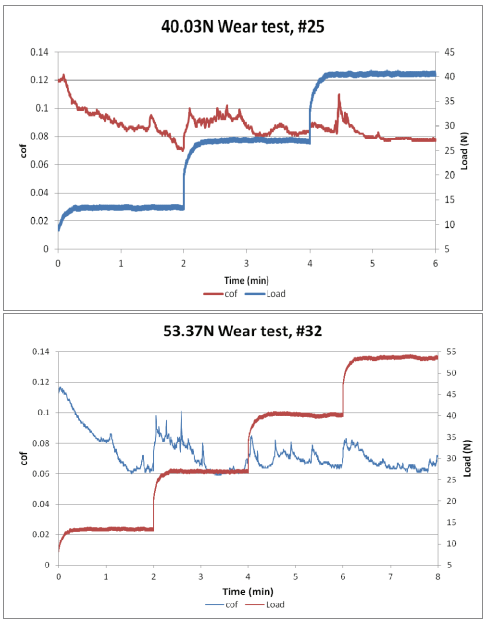

Figure 4: the coefficient of friction and load versus time for 40.03 N and 53.37 N wear tests.

Materials

The material used for the tests was AISI 4140 alloy steel. This material is widely used in the auto industry for parts such as gears, bolts, couplings, spindles, tool holders, sprockets, oil industry drill collars, and tool joints. The chemical and the material properties are detailed in Tables 1 and 2.

Table 1: Chemical composition limits of 4140 alloy steel.

Carbon	0.36-0.46%
Manganese	0.65-1.1%
Silicon	0.15-0.04%
Phosphorus	0.035% Max
Sulfur	0.04% Max
Chromium	0.75-1.2%
Molybdenum	0.10-0.25%
Vanadium	0.05-0.15%
Iron	Remaining%

Table 2: Physical and Mechanical properties of 4140 alloy steel and lubricant

Nominal Density, lbs./in^3	0.283
Electrical Resistivity, microhm-cm @68°F	22
Thermal Conductivity, Btu/ft./hr./°F @212°F	24.7
Thermal coefficient of Expansion, 1/°F	7.67 x 10^{-6} (68°F to 752°F)
Tensile Strength, ksi	90-148
Elongation %	16-26
Hardness, HRB	87
Kinematic viscosity, cSt, at 40 °C	17.1
Kinematic viscosity, cSt, at 90 °C	4.8

The parts were cut to squares of 50mm by 50mm and 13mm thick. The surface was manually polished using a 240 and 400 grit sand paper to get a random texture on the surface and a surface roughness (Ra) of about 0.2µm. The ball bearing was made of 52100 steel with 62 HRC hardness value and had a diameter of 7.94mm. Four milliliters of Synfluid 4 cSt PAO lubricant were applied to the part for each test.

CONTACT MECHANICS MODEL

The pressure distribution used as the input to the temperature model was obtained using a commercially-available software package, MixedPEHL©. This software package uses contact mechanics theory, along with various properties, to predict contact pressure, lambda ratio, film thickness, pressure distribution, subsurface stresses and strains, contact load ratio, contact area ratio, and sliding wear. Some of the key features of this software are its ability to accept as input actual 3D measurements of surface roughness, along with the ability to consider plastic deformation. These roughness measurements greatly improve the accuracy of the predicted outputs.

The software performs all calculations over a computational domain determined by the Hertzian contact ellipse [11]. For a ball-on-disk example, as in the tests presented in this work, the contact area is a point contact. The contact area is shown below

in Figure 5. The length a is defined as the half-width of the Hertzian contact zone. The length b is defined as the semi-axis of the Hertzian ellipse in the y-direction. All of the simulations were run for 1600 dimensionless time steps using a Mesh Level III, which covers the 128x128 computational domain of (Ye+Y0) x (X0+Xe) [11]. For a simulation with an applied load of 53.37 N, a velocity of 1.6 m/s, and a ball with a radius of curvature of 3.97 mm, the actual dimensions of the contact area and computational domain are shown in Figure 6.

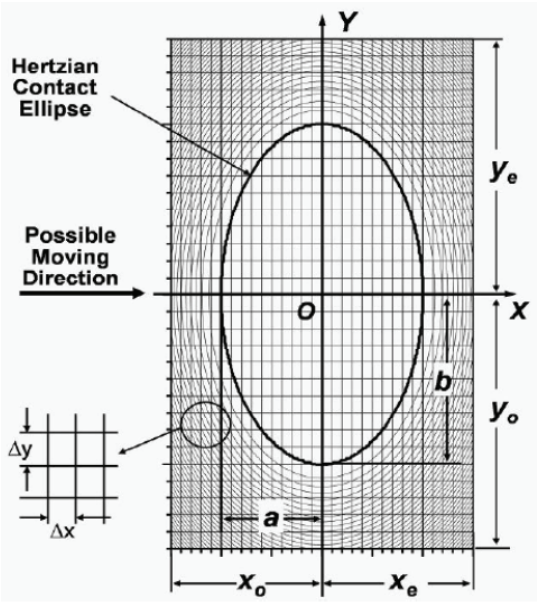

Figure 5: Contact Area and Computational Domain in MixedPEHL (Taken from ContactSim User's Manual [11])

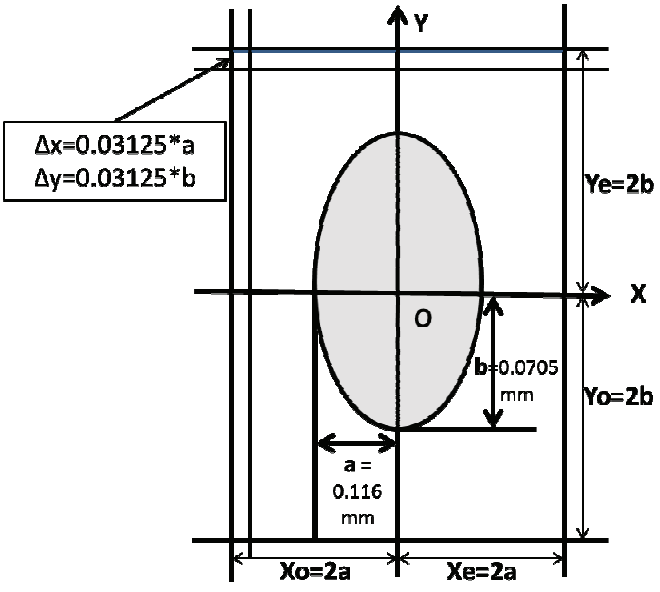

Figure 6: Dimensions of contact area and computational area

The model which governs the performance of the MixedPEHL© software is based on the deterministic mixed EHL model introduced by Hu and Zhu [12] and Zhu and Hu [13]. The model has been extended to include material plasticity of the asperities and base material. All lubrication regimes, including full-film, mixed lubrication, and dry contact, can be accurately modeled [14]. The Reynolds equation is applied to the areas where asperities are in contact, as well as to hydrodynamic regions [15]. When solving the Reynolds equation (1), the pressure boundary condition must be satisfied. At the edges of the solution domain, the pressure must equal zero. Also, a normal cavitation condition must be satisfied at the outlet [14]. The direction in which the ball is rolling is considered to be the x-coordinate.

$$\underbrace{\frac{\partial}{\partial x}\left(\frac{\rho}{12\eta^*}H^3\frac{\partial p}{\partial x}\right)+\frac{\partial}{\partial y}\left(\frac{\rho}{12\eta^*}H^3\frac{\partial p}{\partial y}\right)}_{Pressure\ Flows} = \underbrace{U\frac{\partial(\rho H)}{\partial x}}_{Entraining\ Flow} + \underbrace{\frac{\partial(\rho H)}{\partial t}}_{Squeeze\ Flow} \quad (1)$$

The viscosity of the lubricant is modeled using the Barus law, where p is the pressure [14]:

$$\eta = \eta_0 e^{\gamma p} \quad (2)$$

The lubricant density, a function of pressure, is calculated using the equation from Dowson and Higginson [16,14]:

$$\rho = \rho_0\left(1+\frac{0.6*10^{-9}p}{1+1.7*10^{-9}p}\right) \quad (3)$$

The gap, or local lubricant film thickness H, can be found using the following calculation [14]:

$$H = \underbrace{\frac{h_0(t)}{Original\ Film\ Thickness}}_{} + \underbrace{\frac{\frac{x^2}{2R_x}+\frac{y^2}{2R_y}}{Original\ Geometry}}_{} + \underbrace{\frac{\partial_1(x,y,t)+\partial_2(x,y,t)}{Surface\ Roughness}}_{} + \underbrace{\frac{V(x,y,t)}{Elastic\ Deformation}}_{} + \underbrace{\frac{v_p(x,y,t)}{Plastic\ Deformation}}_{} \quad (4)$$

The Boussinesq integral is used to find the surface elastic deformation [14]:

$$W(x,y,t) = \frac{2}{\pi E'}\iint \frac{p(\xi,\varsigma)}{\sqrt{(x-\xi)^2+(y-\xi)^2}}\mathrm{d}\xi d\varsigma\,, \quad (5)$$

and a volume integration proposed by Jacq et. al. [17] and Chen et. al [18,19] can be used to find the residual surface displacement from subsurface plastic strain [14]:

$$v_p(x,y,t) = 2\mu\iiint_W {\varepsilon_{ij}}^P(\xi,\varsigma,\varphi,t){\varepsilon_{ij}}^e\big(\xi-x,\varsigma-y,\varphi,t\big)d\xi d\varsigma d\varphi \quad (6)$$

Solving equations (1),(4),(5) and (6) simultaneously results in the pressure distribution over the computational domain, as shown in Figure 7. For regions of asperity contact, the thickness of the lubricating film will become practically zero. In these regions, all of the hydrodynamic terms in eq.(1) are equal to zero and the Reynolds equation reduces to [15]:

$$U\frac{\partial H}{\partial x}+\frac{\partial H}{\partial t}=0 \quad (7)$$

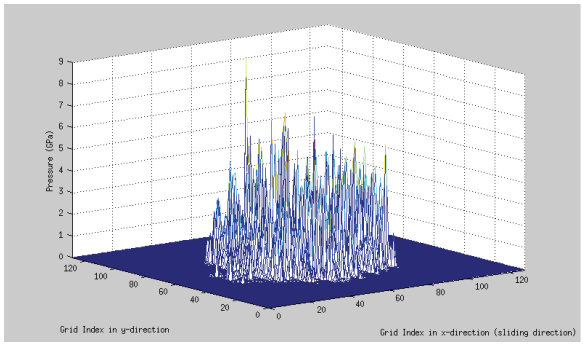

Figure 7: Pressure Distribution in contact area for a Ball-on-Disk Simulation with a 53.57 N Applied Load

THERMAL NUMERICAL METHOD

As indicated earlier, a multiscale modelling approach was used for the computational temperature prediction. First, an average contact pressure is used in simulations of the evolution of the three-dimensional temperature of the sample during a test. Results from this first model, along with the pressure distribution in the contact area obtained from the contact mechanics model are then used in a second 3-D simulation that focuses on a much smaller computational domain in the vicinity of the contact area and computes the evolution of the higher, local flash temperature over very short periods of time.

Bulk Temperature simulations

The commercial finite-element-based multiphysics software, Comsol®, was used for the thermal simulations. Comsol® provides a finite element-based, GUI platform for the modeling and simulation of physics-based problems. It includes several modules that allow for the coupling of various multiphysics phenomena, including mechanical, fluid, chemical and electrical; the heat transfer module, which allows for conduction, convection and radiation calculations was used for this study.

The inputs required by the bulk model come from the contact mechanics simulation, experimental tests and material properties. In this case the evolution of the temperature of the whole sample, a square of 50 by 50 mm and 13 mm thick, was modelled for 120 seconds per load. Figure 8 shows the geometry and the tetrahedral mesh used. The simulation uses the same step loads and velocities as in the experimental tests. The output is a 3D temperature distribution on the part and a bulk temperature value that will be used by the flash temperature model.

The bulk model was based on the transient heat equation in solids:

$$\rho\, C_p \frac{\partial T}{\partial t} + \rho\, C_p\, \mathbf{u} \cdot \nabla T = \nabla\,(k\, \nabla T) \qquad (8)$$

Where ρ is the density (kg/m^3), C_p is the specific heat at constant pressure (J/(kg*K)), T is absolute temperature (K), k is the thermal conductivity (W/m.K) and **u** is the velocity vector (m/s). The four sides (±x, ±y) and the bottom (-z) of the sample were considered to be thermally insulated:

$$-\mathbf{n} \cdot (-k\, \nabla T) = 0 \qquad (9)$$

As shown in Figure 9, a boundary heat source was defined on the top surface (+z) of the sample:

$$-\mathbf{n} \cdot (-k\, \nabla T) = \mathrm{Q}_b \qquad (10)$$

where for each step load, Q_b was defined in the contact area as

$$\mathrm{Q}_b = \mathrm{COF} \times \mathrm{P} \times \mathrm{V} \qquad (11)$$

and on the remainder of the top surface, a convection boundary condition was used

$$\mathrm{Q}_b = \mathrm{h}(\mathrm{T}_\infty - \mathrm{T}), \qquad (12)$$

where P is the contact pressure, V the sliding velocity, h the convective hear transfer coefficient and T_∞ is the ambient temperature. The initial temperature value for the whole domain was equal to the external temperature, in this case 295.30 K.

The mesh created for the bulk model was uniform with a 0.5 element ratio, shown in Figure 8. The element ratio was introduced to create a finer mesh on the contact area (shown with a red circle) while maintaining a coarser where temperature gradients are low. A grid independence study was conducted and it was determined that a mesh with 80×80×20 elements was adequate for the bulk temperature model. A variable-order (two to four), variable-step-size BDF scheme was used for time integration with a minimum time step size of 0.02 s and a maximum of 1 s.

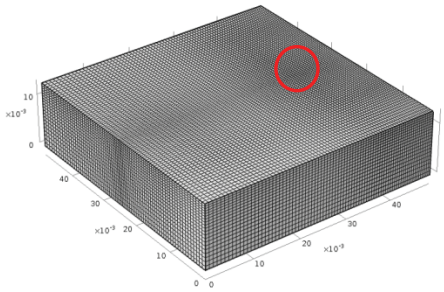

Figure 8: Computational domain and mesh for bulk model

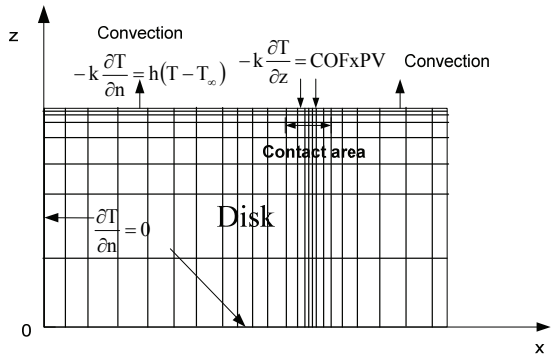

Figure 9: Boundary conditions for bulk model

As seen in Figure 7, the pressure distribution in the contact area output by the contact mechanics model is output on a 128×128 grid in the contact area and is very non-uniform. The grid size used in that data is much smaller than that used in the bulk temperature model. Hence, an average uniform pressure was assumed in the contact area for the first thermal model. In order to ensure that the correct amount of energy was input in the contact area, regardless of grid size used, a correction factor was defined as

$$Correction\ Factor = \frac{P\_file\_average * Contact\ Area}{\int p\_file\_unif(x,y)dA} \quad (13)$$

Where $P\_file\_average$ represent the average value of pressures given by the contact mechanics model pressure file, $Contact\ Area$ represents the area on which the pressure file was applied, and $\int p\_file\_unif(x,y)dA$ is an integral value that has to be calculated in the Comsol® model. It integrates the uniform pressure file over the contact area using the actual grid, which is related to the energy input the model would read with that mesh size without the correction factor.

While this first numerical model provided a transient three-dimensional temperature distribution throughout the body, an average bulk temperature at a given time (say at the end of a test) was needed as an input for the second, flash temperature model. The bulk temperature was defined here as the average temperature of the points in the wear track that are right before the contact zone, as shown in Figure 10. Figure 11 shows an example of the temperature on the circular wear track at five different times, and the temperature value that was selected, in the red rectangle, for the bulk temperature. It was observed that the temperature on the sample increased during the test but it was almost uniform along the circular wear track. The temperature peaks at the beginning and end of Figure 11 represent the elements in the contact area. Note however that these "contact" values do not properly account for the non-uniform contact pressure due to the larger element size used. Hence, the temperature distribution in the contact area has to be calculated using the second flash temperature numerical model which focuses on a much smaller domain involving the contact area.

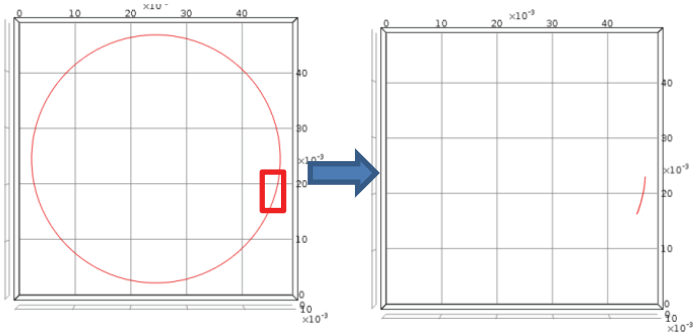

Figure 10: Points of the wear track (shown in red) selected to calculate the bulk temperature

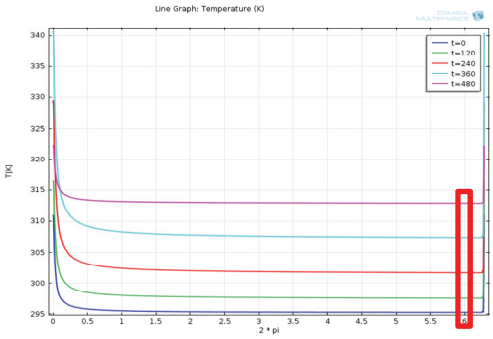

Figure 11: Temperature around the wear track at different times for a 53.37 N wear test; the x-axis shows the angle in radians of points along the wear track, where an angle of zero represents the contact area.

Flash temperature simulations

The flash temperature model took the bulk temperature calculated before as an input, together with operational conditions, material properties and some outputs of the contact mechanics model. In this case the Comsol® computational domain was much smaller since the influence of the rest of the part was considered in the bulk temperature model. A 3-D computational domain of about 1.5 mm×0.6 mm ×0.1mm (Figure 12) was simulated for the time that it takes for an area that came in contact with the ball to movein the x-direction by the equivalent of the length 2b (see Figure 6), i.e., the length of the contact zone in the x-direction. Since the domain was so small and the time duration very short, the effect of curvature could be neglected and movement could approximated as translation (sliding) in the x-direction. The mesh was uniform and significantly finer than the one in the bulk model. The specific size of the domain in the x, y and z directions was slightly different for each sample tested; it was defined by the grid size from the pressure file provided by the contact mechanics model (see Table 3): 178Δx, 114Δy, 25Δz. A generalized alpha time stepping scheme was used with a constant time step size Δt=Δx/V where V is the sliding velocity.

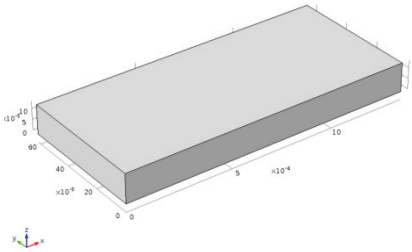

Figure 12: Three-dimensional domain used in the flash temperature model.

The flash model was based on the same governing equations (8)-(12) as the bulk model. There were however some key differences. First, the pressure in the contact area was no longer assumed to be uniform. Instead, a non-uniform pressure distribution (such as the one shown in Figure 7) was used. Second, the contact area was assumed to move with a velocity V in the positive x-direction; this had to be taken into account when identifying the top surface elements at each time step that were subjected to contact versus the ones that experienced convection heat transfer. Last but not least, the temperature of the domain was initialized to the calculated bulk temperature for each step load.

RESULTS AND DISCUSSION

Table 3 summarizes the parameters input into the thermal models for four different wear tests as described before. The coefficient of friction used was an average value for the specific step load. Given that the contact mechanics model outputs

dimensionless normalized pressures in the contact area, the values in each pressure file were multiplied by the corresponding Hertzian pressure, P_h, to determine the actual pressures The average pressure, P_{avg}, which was used in the bulk temperature numerical model was calculated as an average value of all the values in the pressure file. P_{max} represents the maximum (peak) pressure value in the pressure file. Δx, Δy, Δz represent the grid size used in the contact mechanics and flash temperature models.

Table 3: Summary of inputs for the thermal models.

Load [N]	**13.34**	**26.69**	**40.03**	**53.37**
COF[]	0.078	0.08	0.082	0.068
Hertzian P_h[GPa]	1.5118352	1.9157736	2.3462959	2.3843962
P_{avg} [GPa] (bulk)	0.1299982	0.1330967	0.1310582	0.1308738
P_{max}[GPa] (flash)	16.3	12.6	5.12	5.8
Δx[mm]	0.0024328	0.0030725	0.0036131	0.0038516
Δy= Δz [mm]	0.0016919	0.0021141	0.0022019	0.0027103

Bulk temperature simulations

Figure 13 shows the bulk temperature distribution on the top surface of the 4140 steel workpiece at the end of each step load (given in Figure 4) for a 53.37 N wear test. The temperature of the sample is seen to increase over time. The location of contact with the ball, which can be seen as a localized hot spot around the 3 O'clock location in each figure, exhibits a higher temperature than the rest of the sample. However, the temperature can be seen to drop quite rapidly shortly after the workpiece goes through that point (see Figures 11 and 13). The wear track, which can be identified through a faint circular path in each figure, exhibits a slightly higher temperature than the rest of the sample. However, as one approaches the 12 O'Clock, 9 O'Clock and 6 O'clock locations (as the workpiece rotates in a counter-clockwise direction), the temperature in the track area can be seen to approach the temperature of the rest of the top surface.

Table 4 summarizes the bulk wear path temperatures calculated at the end of each step load and Figure 14 plots these bulk temperatures as a function of time. The bulk temperatures were calculated using the elements identified in Figures 10 and 11. As might be expected, the bulk temperatures increase with time. The increase though is non-linear as the COF and contact pressure values vary as the load is varied (Table 3). While the average COF values obtained from the experimental testing are relatively constant and generally below a value of 0.1 until scuffing occurs, they do not necessarily increase or decrease with load. Note for instance the decrease in the COF value in this case as the load is stepped up to 53.37 N. This decrease however may not necessarily be seen with every sample tested due to small differences in surface finish and roughness.

Table 4: Bulk temperatures at the end of each step load for a 53.37N wear test.

Time (s)	Bulk Temperature (K)
0	295.30
120	297.57
240	301.70
360	307.45
480	312.85

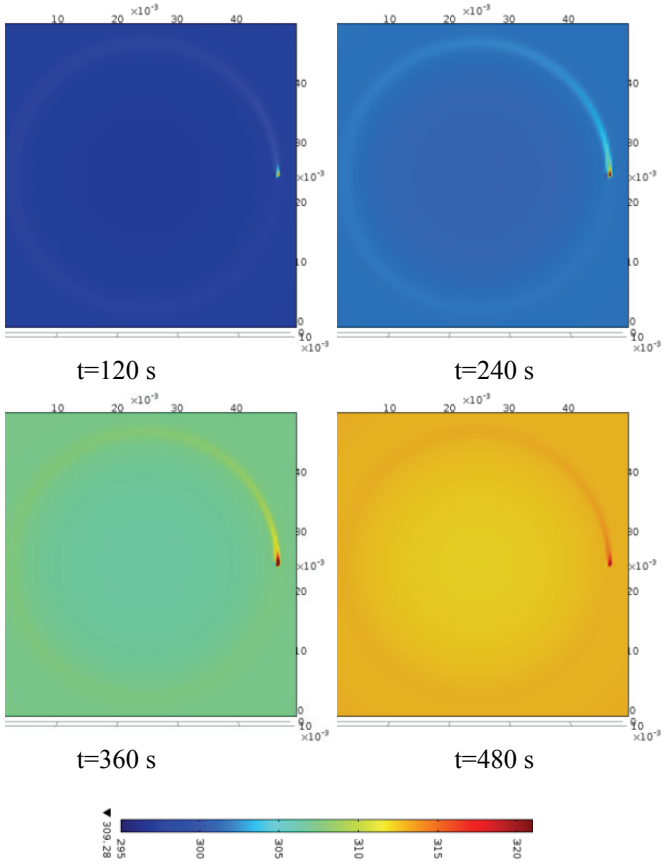

Figure 13: Temperature distribution on the surface at the end of each step load for a 53.37 N wear test

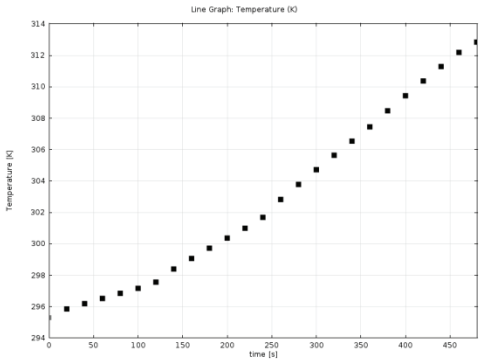

Figure 14: Evolution of bulk temperature for a 53.37 N wear test.

Figure 15 shows a vertical cross section (x-z plane) of the sample at the end of the 53.37 N wear test. The contact area can

be seen as small hot spot very close to the top surface. Figure 16 shows a zoomed in view of the area close to the surface. The thickness of the domain was 13 mm in the z-direction and one can see that the temperature decreases very rapidly in that direction, indicating that the temperature rise is primarily a localized, surface phenomenon. To investigate this further, the second thermal model was used to examine the evolution of the temperature distribution in the vicinity of the contact area.

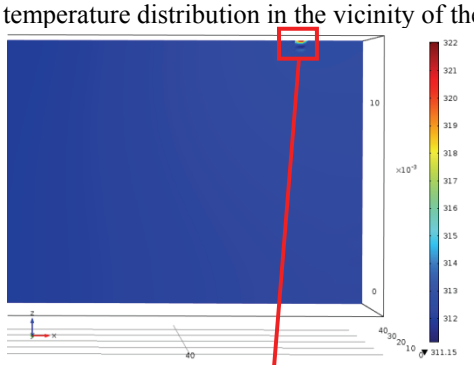

Figure 15: Temperature distribution through a vertical cross section of the sample at the end of a 53.37 N wear test.

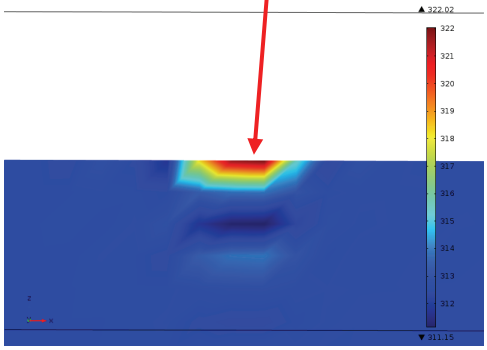

Figure 16: Close-up of bulk temperature model temperature distribution near the contact area at the end of a 53.37 N wear test.

Flash temperature simulations

The bulk temperatures shown in Table 4 and the contact mechanics model values shown in Table 3 were input to the flash temperature numerical model to simulate the temperature evolution in the vicinity of contact area at the end of each step load. Figure 17 illustrates such a temperature evolution on the top surface of the workpiece for a 53.37N load. A time of zero here is equivalent to a time of 480 s (at the end of the step load) and the location of contact can be seen to shift to the right (positive x-direction) with a velocity V=1.6 m/s. In the contact area, the non-uniform contact pressure, as illustrated in Figure 7 is applied. Due to the small grid and time step sizes used, the simulated time is very short (on the order of 0.3 ms) and is equivalent to the contact area shifting by a distance equal to its length, i.e., about 0.5 mm.

As can be noted from Figure17, the temperature distribution in the contact area is not uniform, displaying localized hot spots where the temperature exceeds 500K. This is due to the non-uniform pressure distribution input to the model. As noted in Table 5, the maximum temperature in this case reaches over 535 K, i.e., a maximum surface temperature rise of over 220K in less than 0.3 s. Yet, as seen in the progression of plots in Figure 17, the surface temperature drops rapidly after the contact area shifts away. The rapid rise and drop in the surface temperature upon contact with the ball and subsequent loss of contact is even more readily noticeable in Figure 18 which shows the temperature distribution at different times along an x-direction line in the middle of the top surface of the domain. Temperature changes on the order of 100+K can be observed in very short time periods.

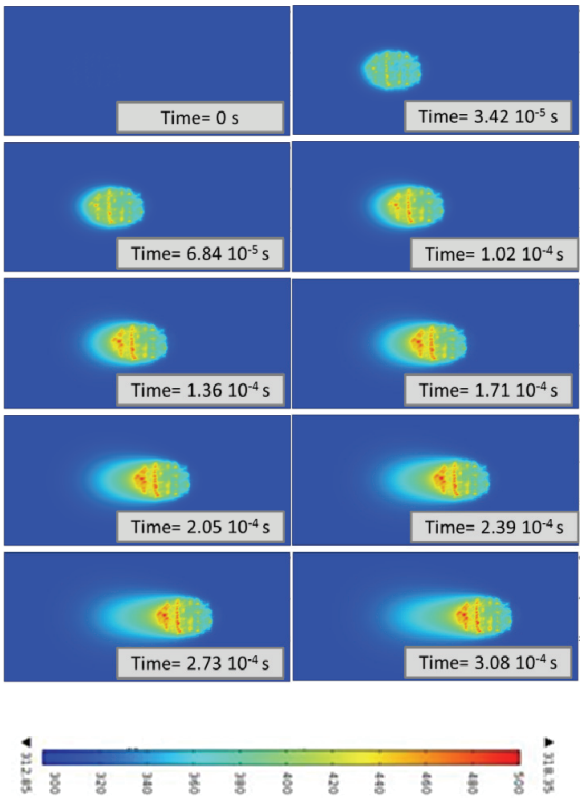

Figure 17: Evolution of temperature in the contact area at the end of a 53.37 N wear test (Flash temperature simulation).

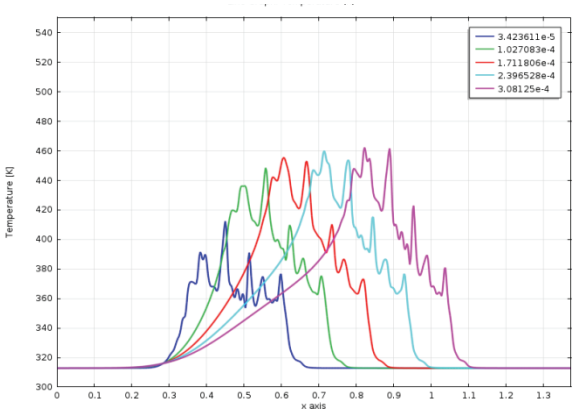

Figure 18: Temperature evolution along a cross-section of the top surface at the end of a 53.37 N wear test (Flash temperature simulation).

Our analysis of the bulk temperature simulations indicated that the temperature rise appeared to be a surface phenomenon. This

is further confirmed by the results of the flash temperature simulations shown in Figure 19 which show a rapid decline in the temperature as one goes below the surface (same temperature scale as Figure 17). In fact, at a depth of about 27 μm, the temperature is almost uniform. This can be explained by the fact that the time that it takes for heat to diffuse a distance d into the material is on the order of d^2/α, where α is the thermal diffusivity of the material, so in the case of the 4140 steel material considered in these simulations, it would take about 0.87 ms for heat to diffuse a distance of about 0.1 mm into the material, which is still a longer time than the time scales considered here.

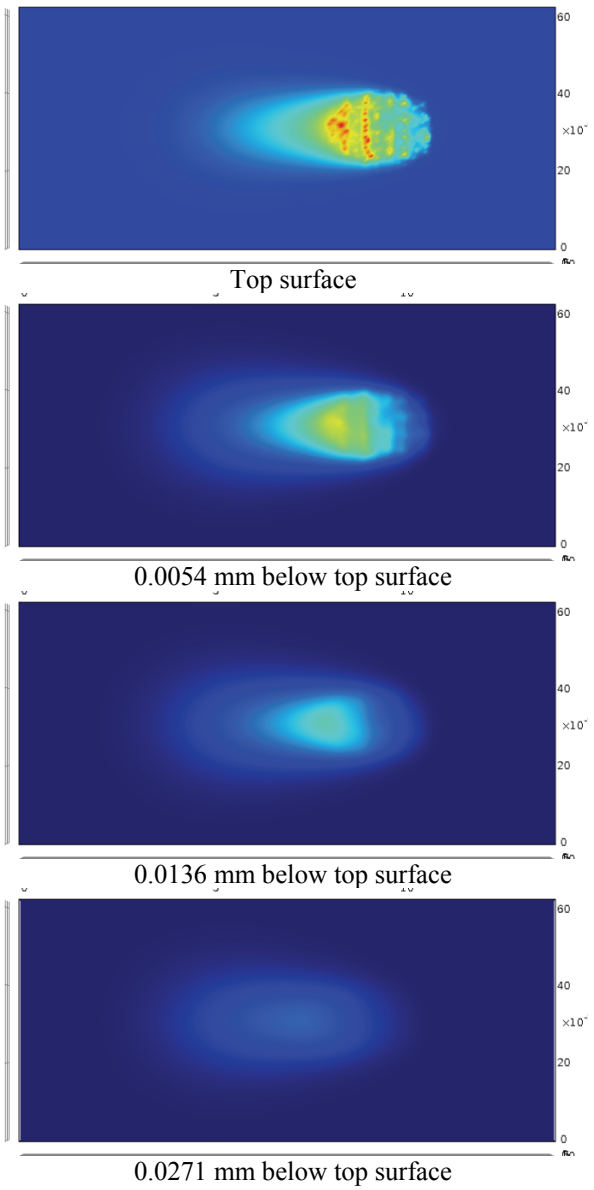

Figure 19: Temperature distribution at 4 different depths.

Additional simulations were performed under other loading conditions. As expected, the lower loading cases generally resulted in lower average surface temperature rises. However, as shown in Table 5, the 26.69N and 40.03N step load cases yielded higher maximum surface temperatures (though lower average surface temperatures) than the higher load case. As shown in Table 3, this can be explained by the fact that these two specific cases had higher coefficients of friction and higher average contact pressures that the 53.37N load case. The 26.69N load case also had a higher maximum pressure (which was applied to one element only but still resulted in a higher local heat input). Yet, it is worth noting that the experimental testing and contact mechanics model showed variability in the coefficient of friction value and maximum contact pressure at a given loading condition.

Table 5: Maximum and average surface temperatures at the end of each step load for a 53.37N wear test (Flash temperature simulation).

Load [N]	T_{max} [K]	T_{avg} [K]
13.34	535.95	300.52
26.69	662.57	306.01
40.03	596.66	313.44
53.37	537.48	316.99

CONCLUSIONS

This paper reported on the development of a numerical thermal model that makes use of data from experimental ball-on-disk tribometer tests and numerical contact mechanics simulations to predict the transient temperature rise on the surface of and within a workpiece. A multiscale approach was used to the simulation of the temperature rise in the workpiece during a ball-on-disk test: first, a bulk temperature of the sample was determined using an average contact pressure and a coarser mesh. This bulk temperature was then used as an input to a finer mesh thermal simulation that incorporated non-uniform contact pressure distributions and focused on the vicinity of the contact area. While the bulk temperature rise at the end of a 53.37N wear test was found to be on the order of 17 K, much larger temperature rises (on the order of 200 K or more) were observed in the contact area using the flash temperature numerical model. The rapid surface temperature increases in the area of contact were also followed by rapid temperature decreases as the source of frictional heat input moved away. The temperature was also found to change less significantly below the surface, indicating that the temperature rise due to contact is primarily a surface phenomenon.

All of our simulations so far have focused on the period prior to scuffing. The next step of this study is to extend these simulations to many more loading cases to see if they can help shed some light on the temperature rise that occurs during scuffing processes. Furthermore, while the temperature increases calculated are still modest enough to not significantly impact the mechanical material properties of the material, they may be high enough to affect the viscosity of any lubricant between the ball and workpiece and hence affect the Sample results for both the bulk disk temperature, as well as the contact mechanics and contact pressure distribution. Hence, future work may also focus on modifying the inputs to the contact mechanics model in view of the temperature results to see what effect this may have on stress, strain and pressure.

ACKNOWLEDGMENTS

This material is based upon work supported by the U.S. Army TACOM Life Cycle Command under Contract No. W56HZV-08-C-0236, through a subcontract with Mississippi State University, and was performed for the Simulation Based Reliability and Safety (SimBRS) research program. Any opinions, findings and conclusions or recommendations expressed in this material are those of the author(s) and do not necessarily reflect the views of the U.S. Army TACOM Life Cycle Command.

REFERENCES

[1] J. Hershberger et al, Evidence of scuffing initiation by adiabatic shear instability, Wear 258 (2005) 1471-1478

[2] W. F. Bowman and G. W. Stachowiak, A review of scuffing models, Tribology Letters 2 (1996) 113-131

[3] H. Blok, Theoretical study of temperature rise at surfaces of actual contact under oiliness lubricating conditions, Proc. Gen. Disscuss. Lubr. 2 (1937)222-235

[4] A. Dyson, The failure of elastohydrodynamic lubrication of circumferentially ground discs, Proc. Inst. Mech. Eng. 190 (1976)52-76

[5] J.J. Frewing, The heat adsorption of long-chain compounds and their effect on boundary lubrication, Proc. Roy. Soc. A282 (1944) 270

[6] I. Langmuir,The constitution and fundamental properties of solids and liquids, J. Am. Chem. Soc. 38 (1916) 2221; 39 (1917) 1848

[7] S.M. Hsu et al., Mechano-chemical model: Reaction temperatures in a concentrated contact, Wear 175 (1994) 209

[8] K. C. Ludema, A review of scuffing and running-in of lubricated surfaces, with asperities and oxides in perspective, Wear 100 (1984) 315

[9] A. Jackson and J.C. Enthoven, The effect of lubricant traction on scuffing, STLE 37 (1994) 387

[10] Mikecz, N., Kelley, N., Othman, E., Lumbreras, R. et al., Scuffing Behavior of 4140 Alloy Steel and Ductile Cast Iron, *SAE Int. J. Mater. Manf.* 5(1):122-129, 2012, doi:10.4271/2012-01-0189.

[11] Tri-Tech Solutions ContactSim© Help, www.Tri-Tech-Solutions.com

[12] Hu, Y.Z., and Zhu, D., 2000, "A Full Numerical Solution to the Mixed Lubrication in Point Contacts," ASME J. Tribol., **122**(1), pp.1-9.

[13] Zhu, D., and Hu, Y.Z., 1999, "The Study of Transition From Full Film Elastohydrodynamic to Mixed and Boundary Lubrication," *The Advancing Frontier of Engineering Tribology,* Proceedings of the 1999 STLE/ASME H. S. Cheng Tribology Surveillance, pp.150-156.

[14] Ren, N., Zhu, D., Chen, W. W., and Wang, Q. J., 2010, "Plasto-Elastohydrodynamic Lubrication (PEHL) in Point Contacts," ASME J. Tribol., 132 , p. 031501.

[15] Hu, Y. Z., Wang, H., Wang, W. Z., and Zhu, D., 2001, "A Computer Model of Mixed Lubrication in Point Contacts," Tribol. Int., 34 , pp. 65–73.

[16] Dowson, D., and Higginson, G.R., 1966, *Elastrohydrodynamic Lubrication*, Pergamon, Oxford, UK.

[17] Jacq, C., Nelias, D., Lorman, G. and Girodin, D., 2002, "Development of a Three-Dimensional Semi-Analytical Elastic-Plastic Contact Code," ASME J. Tribol., **124**, pp. 653-667.

[18] Chen. W. W., Liu, S.B., and Wang, Q., 2008, "Fast Fourier Transform Based Numerical Methods for Elasto-Plastic Contacts With Nominally Flat Surface," ASME J. Appl. Mech., **75**, p. 011022.

[19] Chen, W. W., and Wang Q., 2008, "Thermomechanical Analysis of Elasto-Plastic Bodies in a Sliding Spherical Contact and the Effects of Sliding Speed, Heat Partition, and Thermal Softening," ASME J. Tribol., **130**, p. 041402.

NOMENCLATURE

a [mm] radius of Hertzian contact ellipse in x-direction
α [m^2/s] Thermal diffusivity
γ [GPa^{-1}] Pressure-viscosity exponent used in Barus law
C_p [J/kg.K] Specific heat
E [GPa] Young's modulus of material
H [nm] local film thickness/gap between surfaces
h [$W/m^2.K$] Convective heat transfer coefficient
k [W/m.K] Thermal conductivity
p, P [GPa] pressure
P_h [GPa] maximum Hertzian pressure
b [mm] semi-axis of the Hertzian ellipse in the y-direction
Xe [mm] Outlet distance in the rolling direction (x-direction)
X0 [mm] Inlet distance in the rolling direction (x-direction)
Ye [mm] Outlet distance in the y-direction
Y0 [mm] Inlet distance in the y-direction
Δx [mm] Mesh size in x-direction
Δy [mm] Mesh size in y-direction
ρ [g/mL]lubricant density
$\eta*$ [cSt] effective viscocity
U [m/s] $(u_1+u_2)/2$, rolling velocity
η_0 [cSt] viscocity under ambient conditions
ρ_0 [g/mL]density under ambient conditions
$h_0(t)$ [nm] distance between ball and disk at x=0 without adding deformation
R_x [mm] effective radius in x-z plane
R_y [mm] effective radius in y-z plane
x [mm] x-coordinate (location in rolling direction)
y [mm] y-coordinate
∂_1 [microns]Roughness height of surface 1
∂_2 [microns]Roughness height of surface 2
V [m/s] Sliding velocity
W [mm] Elastic surface deformation
v_p [mm] Surface displacement from plastic deformation
E' [GPa] Effective Young's modulus
ξ [mm] x-coordinate for calcualting elastic and plastic deformation
ς [mm] y-coordinate for calculating elastic and plastic deformation
φ [mm] z-coordinate for calculating plastic deformation
T [K] Temperature
t [s] Time